

3D Cable-Based Cartesian Metrology System

Robert L. Williams II

Ohio University
Athens, Ohio

James S. Albus and Roger V. Bostelman

NIST
Gaithersburg, MD

Journal of Robotic Systems

21(5): 237-257, 2004

Keywords: metrology, cable-based metrology, cables, wires, string pots, rapid prototyping, robotics, automated construction.

Contact information:

Robert L. Williams II

Associate Professor

Department of Mechanical Engineering

259 Stocker Center

Ohio University

Athens, OH 45701-2979

Phone: (740) 593-1096

Fax: (740) 593-0476

E-mail: williar4@ohio.edu

URL: <http://www.ent.ohiou.edu/~bobw>

3D Cable-Based Cartesian Metrology System

Robert L. Williams II
Ohio University, Athens, Ohio

James S. Albus and Roger V. Bostelman
NIST, Gaithersburg, MD

ABSTRACT

A novel cable-based metrology system is presented wherein six cables are connected in parallel from ground-mounted string pots to the moving object or tool of interest. Cartesian pose can be determined for feedback control and other purposes by reading the lengths of the six cables via the string pots and using closed-form forward pose kinematics. This article focuses on a sculpting metrology tool, assisting a human artist in generating a piece from a computer model, but applications exist in manufacturing, rapid prototyping, robotics, and automated construction. We present experimental data to demonstrate the operation of our system, we study the absolute accuracy and also measurement resolution, and we discuss various error sources. The proposed real-time cable-based metrology system is less complex and more economical than existing commercial Cartesian metrology technologies.

1. INTRODUCTION

Many applications in robotics, construction, and manufacturing require effective real-time measurement of Cartesian pose of end-effectors, tools, and materials. Current technologies in use for pose metrology include machine vision, photogrammetry, theodolites, laser interferometry, magnetic tracking, stereo optical image registration, and acoustic methods; many of the technologies are complex and expensive. The current article presents a novel system for Cartesian pose measurement using six cables (whose lengths are sensed via passive string pots with torsional-spring tensioning) connected to the end-effector. The proposed system is relatively simple and economical.

This idea is related to cable-suspended robots; the literature in this area is growing, starting with the NIST (National Institute of Standards and Technology) RoboCrane¹ and the McDonnell-Douglas* Charlotte². The kinematics, dynamics, control, and applications of cable-suspended robots are topics of current interest^{3,4,5}.

NIST was also the innovator behind passive cable-based metrology. The Robot Calibrator⁶ used three cables meeting at a single point, measured by three string encoders, and was used to calibrate a PUMA robot, position only. A similar idea was implemented⁷ for partial-pose (position) calibration of an industrial robot, with experimental results. Jeong, et al.⁸, have also implemented a similar cable-based industrial robot pose-measuring system. Their six-cable parallel wire mechanism is based on a (non-inverted) Stewart Platform. No analytical solution to the forward pose

kinematics problem exists; instead they use a numerical approach. SpaceAge Controls, Inc. has used spring-loaded cable/potentiometer position transducers for aircraft applications (such as aileron control) for thirty years (www.spaceagecontrol.com*).

Another unique NIST application of cable-based metrology has been in conjunction with mathematician/sculptor Helaman Ferguson⁹ (www.helasculpt.com*). To provide an innovative tool for assisting a human artist in generating a sculpture from a 3D complex mathematical surface in a computer model, three cable-based metrology systems have been developed. The purpose of these is to provide Cartesian pose feedback for replicating the computer model in real-world materials. The String-Pot 1 System again only provides 3D position feedback to the human, using three cables and string pots meeting in a single point. The String-Pot 2 System allows for full 6-degree-of-freedom (6-dof) pose (position and orientation) feedback to the human. It is basically a passive RoboCrane, an inverted Stewart platform with six cables and string pots. The sculpting tool is connected to the moving platform of the passive RoboCrane and the human sculptor stands within this moving platform. These systems are documented in Bostelman¹⁰ and Ferguson¹¹.

The third cable-based metrology sculpting tool, developed at NIST, is the subject of this article. Like the String-Pot 2 System, the current concept provides 6-dof pose measurement; however, the design has been changed from the symmetric RoboCrane-like structure to improve pose measurement and human interaction. The next section presents the system description for this Six-Cable Hand-Directed Sculpting System. The forward pose kinematics problem is important for calculating poses given the six sensed cable lengths; an analytical solution to the forward pose kinematics problem for the NIST system is presented. This article also presents various kinematics issues including sculpting displacements for display to the human, Cartesian measurement uncertainty, calibration of fixed cable points, and workspace. We then present experimental data to demonstrate the effectiveness of our system; we then consider accuracy and error sources. Sculpting metrology is an interesting application; however, various potential applications exist for this NIST cable-based metrology technology, including manufacturing, rapid prototyping, robotics, and automated construction. This type of metrology system is adaptable to large-scale problems.

2. SYSTEM DESCRIPTION

Figure 1 shows the arrangement of the six-cable hand-directed sculpting system. The system is large: it stands almost 4.3 m (14 *ft.*) high and is supported by three 55-gallon drums on an equilateral triangle of side 3.0 m (10 *ft.*). The size and height of the sculpting tool is exaggerated in Figure 1 for clarity. Figure 2 shows a photograph of the supporting frame.

In Figure 1, the (irregular) tetrahedral base frame has vertices A , B , C , and D ; the vertices of the moving, hand-directed tool are P_1 , P_2 , and P_3 , and the cutting tip T is located at the origin of moving frame $\{T\}$. The world coordinate frame is $\{0\}$; the origin of this frame is on the floor and directly under point C along the Z axis.

* The identification of any commercial product or trade name does not imply endorsement or recommendation by Ohio University or NIST.

The lengths of the six cables are L_i , $i = 1, 2, \dots, 6$. Fixed points C_1 , C_2 , C_3 , A_4 , A_5 , and B_6 are the cable contact points on the ground-mounted string pots, located near points C , A , and B , respectively. Cable 1 connects C_1 to P_1 , cable 2 connects C_2 to P_2 , cable 3 connects C_3 to P_3 , cable 4 connects A_4 to P_3 , cable 5 connects A_5 to P_2 , and cable 6 connects B_6 to P_2 . The sides of the rigid moving platform triangle are s_1 , s_2 , and s_3 .

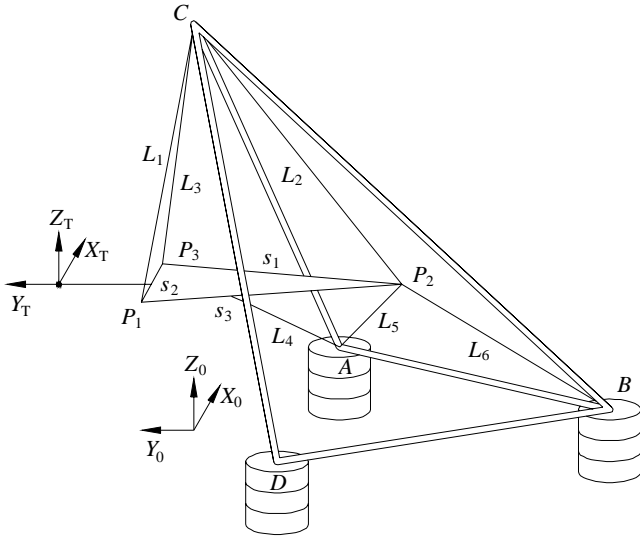


Figure 1. Six-Cable Metrology System Diagram



Figure 2. Six-Cable Metrology System Photograph

Figure 3 shows a photograph of the aluminum cross with eyebolts, representing the sculptor's chainsaw in the NIST hardware. Moving cable connection points P_1 , P_2 , and P_3 are shown, with one, three, and two cables connecting, respectively. The tip of the cross is the origin of the tool-tip frame $\{T\}$. We assume that points P_1 , P_2 , and P_3 are known in the $\{T\}$ frame and then points C_1 , C_2 , C_3 , A_4 , A_5 , and B_6 are known in the $\{0\}$ frame.

Figure 4 shows one of the six string pots, which are 10-turn potentiometers for measuring the length of each cable. These string pots allow a length change of 2.54 m (100 inches) and are linear over their operating range. A torsional spring maintains tension (about 2 N) on the cable at all times.



Figure 3. Chainsaw Proxy



Figure 4. String Pot

3. FORWARD POSE KINEMATICS

Forward pose kinematics is required for Cartesian metrology over time. Given the six cable lengths read from the string pots, we calculate the Cartesian pose (three translations and three rotations) in this section. First, we derive a closed-form solution. Due to the fact that the fixed cable points vary slightly as the cables rotate at different angles over their respective string pot pulleys (see Figure 4), this solution has some error; this is then corrected by an iterative solution, using the basic closed-form solution at each step.

3.1 Nominal Closed-Form Solution

The forward pose kinematics problem is stated: Given the six cable lengths L_i , $i=1,2,\dots,6$, calculate the Cartesian pose of the chainsaw tip frame, expressed by homogeneous transformation matrix $\begin{bmatrix} 0 \\ T \end{bmatrix} \mathbf{T}$ or the six Cartesian pose numbers $\{^0 \mathbf{X}_T\} = \{x \ y \ z \ \alpha \ \beta \ \gamma\}^T$ (we use $ZYX \ \alpha\beta\gamma$ Euler angles¹²). This pose can then be interpreted and used for the sculpting or other Cartesian task at hand. Unlike many parallel robot forward pose kinematics problems, there exists a closed-form solution, and the computation requirements are not demanding. There are multiple solutions, but the correct solution can generally be determined.

The system in Figure 1 can be viewed as a (non-symmetric) 3-2-1 Stewart Platform, whose forward pose kinematics problem has been presented^{13,14,15}.

The forward pose kinematics solution consists of finding the intersection point of three given spheres; this must be done three times in the following sequence. Let us refer to a sphere as a vector center point \mathbf{c} and scalar radius r : (\mathbf{c}, r) . Moving points P_i are found first, represented by vectors expressed in $\{0\}$: ${}^0 \mathbf{P}_i$, $i=1,2,3$.

1. P_2 is the intersection of: $({}^0 \mathbf{A}_5, L_5)$, $({}^0 \mathbf{B}_6, L_6)$, and $({}^0 \mathbf{C}_2, L_2)$.
2. P_3 is the intersection of: $({}^0 \mathbf{A}_4, L_4)$, (P_2, s_1) , and $({}^0 \mathbf{C}_3, L_3)$.
3. P_1 is the intersection of: (P_2, s_3) , (P_3, s_2) , and $({}^0 \mathbf{C}_1, L_1)$.

Where s_1 , s_2 , and s_3 are the known fixed lengths of the moving platform: $s_1 = \|P_2 P_3\|$, $s_2 = \|P_3 P_1\|$, and $s_3 = \|P_1 P_2\|$ (see Figure 1).

The closed-form intersection of three given spheres algorithm is given below, but let us first finish the forward pose kinematics solution, assuming ${}^0 \mathbf{P}_i$ are now known. Given ${}^0 \mathbf{P}_i$, we can calculate the orthonormal rotation matrix $\begin{bmatrix} 0 \\ P_i \end{bmatrix} \mathbf{R} = \begin{bmatrix} 0 \\ P_i \end{bmatrix} \mathbf{R}$ directly (we assume that frames $\{P_1\}$, $\{P_2\}$, $\{P_3\}$ (coordinate frames placed at points P_i), and $\{T\}$ frames have identical orientation), using the definition¹² that each column of this matrix expresses one of the XYZ unit vectors of $\{T\}$ (or $\{P_i\}$) with respect to $\{0\}$:

$$\begin{bmatrix} {}^0\mathbf{R}_{P_i} \end{bmatrix} = \begin{bmatrix} | & | & | \\ {}^0\hat{X}_{P_i} & {}^0\hat{Y}_{P_i} & {}^0\hat{Z}_{P_i} \\ | & | & | \end{bmatrix} \quad (1)$$

The columns for (1) are calculated using (2), referring to Figure 1.

$${}^0\hat{X}_{P_i} = \frac{{}^0\mathbf{P}_3 - {}^0\mathbf{P}_1}{\|{}^0\mathbf{P}_3 - {}^0\mathbf{P}_1\|} \quad {}^0\hat{Y}_{P_i} = \frac{{}^0\mathbf{P}_4 - {}^0\mathbf{P}_2}{\|{}^0\mathbf{P}_4 - {}^0\mathbf{P}_2\|} \quad {}^0\hat{Z}_{P_i} = {}^0\hat{X}_{P_i} \times {}^0\hat{Y}_{P_i} \quad (2)$$

where P_4 (not shown in Figure 1) is the midpoint of P_1P_3 :

$${}^0\mathbf{P}_4 = {}^0\mathbf{P}_1 + \left(\frac{s_2}{2}\right) {}^0\hat{X}_{P_i} \quad (3)$$

There are two solutions to the intersection point of three given spheres (see the following subsection); therefore, the forward pose kinematics problem yields a total of $2^3 = 8$ mathematical solutions since we must repeat the algorithm three times. Generally only one of these is the valid solution for the hand-directed sculpting tool. Also, as seen in the spheres intersection algorithm below, solution singularities exist. These issues will be dealt with later.

3.1.1 Three Spheres Intersection Algorithm. We now derive the equations and solution for the intersection point of three given spheres. This solution is required (three separate times) by the forward pose kinematics solution above. Let us assume that the three given spheres are (\mathbf{c}_1, r_1) , (\mathbf{c}_2, r_2) , and (\mathbf{c}_3, r_3) . That is, center vectors $\mathbf{c}_1 = \{x_1 \ y_1 \ z_1\}^T$, $\mathbf{c}_2 = \{x_2 \ y_2 \ z_2\}^T$, $\mathbf{c}_3 = \{x_3 \ y_3 \ z_3\}^T$, and radii r_1 , r_2 , and r_3 are known (The three sphere center vectors must be expressed in the same frame, $\{0\}$ in this article; the answer will be in the same coordinate frame). The equations of the three spheres are:

$$\begin{aligned} (x - x_1)^2 + (y - y_1)^2 + (z - z_1)^2 &= r_1^2 \\ (x - x_2)^2 + (y - y_2)^2 + (z - z_2)^2 &= r_2^2 \\ (x - x_3)^2 + (y - y_3)^2 + (z - z_3)^2 &= r_3^2 \end{aligned} \quad (4)$$

Equations (4) are three coupled nonlinear equations in the three unknowns x , y , and z . The solution will yield the intersection point $\mathbf{P} = \{x \ y \ z\}^T$. The solution approach is to expand equations (4) and combine them in ways so that we obtain $x = f(y)$ and $z = f(y)$; we then substitute these functions into one of the original sphere equations and obtain one quadratic equation in y only. This can be readily solved, yielding two y solutions. Then we again use $x = f(y)$ and $z = f(y)$ to determine the remaining unknowns x and z , one for each y solution. Let us now derive this solution.

First, expand equations (4) by squaring all left side terms. Then subtract the third from the first and the third from the second equations, yielding (notice this eliminates the squares of the unknowns):

$$a_{11}x + a_{12}y + a_{13}z = b_1 \quad (5)$$

$$a_{21}x + a_{22}y + a_{23}z = b_2 \quad (6)$$

where:

$$\begin{aligned} a_{11} &= 2(x_3 - x_1) & a_{21} &= 2(x_3 - x_2) & b_1 &= r_1^2 - r_3^2 - x_1^2 - y_1^2 - z_1^2 + x_3^2 + y_3^2 + z_3^2 \\ a_{12} &= 2(y_3 - y_1) & a_{22} &= 2(y_3 - y_2) & b_2 &= r_2^2 - r_3^2 - x_2^2 - y_2^2 - z_2^2 + x_3^2 + y_3^2 + z_3^2 \\ a_{13} &= 2(z_3 - z_1) & a_{23} &= 2(z_3 - z_2) & & \end{aligned}$$

Solve for z in (5) and (6):

$$z = \frac{b_1}{a_{13}} - \frac{a_{11}}{a_{13}}x - \frac{a_{12}}{a_{13}}y \quad z = \frac{b_2}{a_{23}} - \frac{a_{21}}{a_{23}}x - \frac{a_{22}}{a_{23}}y \quad (7,8)$$

Subtract (7) from (8) to eliminate z and obtain $x = f(y)$:

$$x = f(y) = a_4y + a_5 \quad (9)$$

where:

$$\begin{aligned} a_4 &= -\frac{a_2}{a_1} & a_5 &= -\frac{a_3}{a_1} \\ a_1 &= \frac{a_{11}}{a_{13}} - \frac{a_{21}}{a_{23}} & a_2 &= \frac{a_{12}}{a_{13}} - \frac{a_{22}}{a_{23}} & a_3 &= \frac{b_2}{a_{23}} - \frac{b_1}{a_{13}} \end{aligned}$$

Substitute (9) into (8) to eliminate x and obtain $z = f(y)$:

$$z = f(y) = a_6y + a_7 \quad (10)$$

where:

$$a_6 = \frac{-a_{21}a_4 - a_{22}}{a_{23}} \quad a_7 = \frac{b_2 - a_{21}a_5}{a_{23}}$$

Now substitute (9) and (10) into the first equation in (4) to eliminate x and z and obtain a single quadratic in y only:

$$ay^2 + by + c = 0 \quad (11)$$

$$a = a_4^2 + 1 + a_6^2$$

where:

$$b = 2a_4(a_5 - x_1) - 2y_1 + 2a_6(a_7 - z_1)$$

$$c = a_5(a_5 - 2x_1) + a_7(a_7 - 2z_1) + x_1^2 + y_1^2 + z_1^2 - r_1^2$$

There are two solutions for y :

$$y_{\pm} = \frac{-b \pm \sqrt{b^2 - 4ac}}{2a} \quad (12)$$

To complete the intersection of three spheres solution, substitute both y values y_+ and y_- from (12) into (9) and (10):

$$x_{\pm} = a_4y_{\pm} + a_5 \quad (13)$$

$$z_{\pm} = a_6y_{\pm} + a_7 \quad (14)$$

In general there are two solutions, one corresponding to the positive and the second to the negative in (12).

Obviously, the + and - solutions cannot be switched:

$$\{x_+ \quad y_+ \quad z_+\}^T \quad \{x_- \quad y_- \quad z_-\}^T \quad (15)$$

Let us now present a simple example to demonstrate the solutions in the intersection of three spheres algorithm. Given three spheres (\mathbf{c}, r) :

$$\left(\{0 \ 0 \ 0\}^T, \sqrt{2}\right), \left(\{3 \ 0 \ 0\}^T, \sqrt{5}\right), \left(\{1 \ -3 \ 1\}^T, 3\right) \quad (16)$$

The intersection of three spheres algorithm yields the following two valid solutions:

$$\{x_+ \ y_+ \ z_+\}^T = \{1 \ 0 \ 1\}^T \quad \{x_- \ y_- \ z_-\}^T = \{1 \ -0.6 \ -0.8\}^T \quad (17)$$

These two solutions may be verified by a 3D sketch. This completes the intersection of three spheres algorithm. In the next subsections we finish the overall forward pose kinematics solution discussion by presenting several important topics: imaginary solutions, singularities, and multiple solutions.

3.1.2 Imaginary Solutions. The three spheres intersection algorithm can yield imaginary solutions. This occurs when the radicand $b^2 - 4ac$ in (12) is less than zero; this yields imaginary solutions for y_{\pm} , which physically means not all three spheres intersect. If this occurs in the hardware, there is either a cable length sensing error or a modeling error, since the hardware assembles properly.

A special case occurs when the radicand $b^2 - 4ac$ in (12) is equal to zero. In this case, both solutions have degenerated to a single solution, i.e. two spheres meet tangentially in a single point, and the third sphere also passes through this point. This can happen in the hardware, for instance when point P_2 lies on plane ABC (see Figure 1), plus either cables L_2L_5 , L_5L_6 , or L_6L_2 are collinear.

3.1.3 Singularities. The three spheres intersection algorithm and hence the overall forward pose kinematics solution is subject to singularities. These are all algorithmic singularities, i.e. division by zero in the mathematics, but no problem exists in the hardware (no loss or gain in degrees of freedom). This subsection derives and analyzes the algorithmic singularities for the three spheres intersection algorithm presented above. Different possible three spheres intersection algorithms exist, by combining different equations starting with (4) and eliminating and solving for different variables first. Each has a different set of algorithmic singularities. We only analyze the algorithm presented above.

Inspecting the algorithm, represented in equations (4) – (15), we see there are four cases in which the algorithm experiences mathematical difficulty (we already discussed the imaginary solutions cases above and do not include them here); all involve division by zero:

Singularity Conditions:

$$\begin{aligned} a_{13} = 0; a_{23} = 0 \\ a_1 = 0; a = 0 \end{aligned} \quad (18)$$

The first two singularity conditions:

$$\begin{aligned} a_{13} &= 2(z_3 - z_1) = 0 \\ a_{23} &= 2(z_3 - z_2) = 0 \end{aligned} \quad (19)$$

are satisfied when the centers of spheres 1 and 3 or spheres 2 and 3 have the same z coordinate, i.e. $z_1 = z_3$ or $z_2 = z_3$. These can occur for the Hand-Directed Sculpting Tool. However, judicious choice of which are numbered spheres 1, 2, and 3 can completely avoid this algorithmic singularity; recall the chosen sphere intersection sequence for overall forward pose kinematics is given early in Section 3.1. The fixed sphere centers ${}^0\mathbf{A}_5$ and ${}^0\mathbf{B}_6$ always have the same z coordinate; therefore in the first step they must appear as spheres 1 and 2. In the second step, sphere centers ${}^0\mathbf{A}_4$ and P_2 can have the same z coordinate and hence appear as spheres 1 and 2. In the third and final step, moving sphere centers P_2 and P_3 can have the same z coordinate (this case is the nominal horizontal orientation) and hence appear as spheres 1 and 2. In all cases fixed sphere center ${}^0\mathbf{C}_i$, $i=1,2,3$, appears as the third sphere because its z coordinate will never be the same as any of the other fixed and moving sphere centers, for a normal human standing on the ground. Therefore, the algorithmic singularity conditions 1 and 2 pose no problem in the hardware.

The third singularity condition,

$$a_1 = \frac{a_{11}}{a_{13}} - \frac{a_{21}}{a_{23}} = 0 \quad (20)$$

Simplifies to:

$$\frac{x_3 - x_1}{z_3 - z_1} = \frac{x_3 - x_2}{z_3 - z_2} \quad (21)$$

For this condition to be satisfied, the centers of spheres 1, 2, and 3 must be collinear in the XZ plane. For the first use of the three spheres algorithm, fixed centers ${}^0\mathbf{A}_5$, ${}^0\mathbf{B}_6$, and ${}^0\mathbf{C}_2$ are never collinear. For the second use of the three spheres algorithm, it is theoretically possible for the sphere centers ${}^0\mathbf{A}_4$, P_2 , and ${}^0\mathbf{C}_3$ to lie along the same line in the XZ plane. However, in reality, we will define the useful workspace to be bounded by the tetrahedral frame; thus, this type of algorithmic singularity will occur only near the workspace edge AC in the hardware. For the third use of the three spheres algorithm, it is again possible for the sphere centers P_2 , P_3 , and ${}^0\mathbf{C}_1$ to lie along the same line in the XZ plane. In this case line P_2P_3 must also pass through ${}^0\mathbf{C}_1$, which means line P_2P_3 is collinear with the third cable. This case is far from nominal orientation ($\alpha = \beta = \gamma = 0$). Also, we define the boundary of the useful orientation workspace to be when a cable lies along one of the sides of the chainsaw. Hence, singularity condition 3 lies along the edge of the useful workspace and thus presents no problem in the hardware if the user is properly instructed regarding workspace limitations. A singularity-approaching algorithm can be developed to warn the user in these cases.

The fourth singularity condition,

$$a = a_4^2 + 1 + a_6^2 = 0 \quad (22)$$

Is satisfied when:

$$a_4^2 + a_6^2 = -1 \quad (23)$$

It is impossible to satisfy this condition as long as a_4 and a_6 (from (9) and (10)) are real numbers (this is the case in the hardware). Thus, the fourth singularity condition is never a problem in the sculpting tool hardware.

To summarize, this subsection analyzes the algorithmic singularity conditions for the three spheres intersection algorithm as applied to forward pose kinematics of the Hand-Directed Sculpting Tool. Four singularity conditions were found and none present problems for the forward pose solution. Only one subcase of the four was found to be a potential problem, but it lies on the boundary of the useful workspace. To reach this conclusion, it was also important to order the spheres passed into the algorithm properly.

3.1.4 Multiple Solutions. In general the three spheres intersection algorithm yields two distinct, correct solutions (\pm in (12-14)). Since this algorithm is used three times in the overall forward pose kinematics solution, $2^3 = 8$ valid mathematical solutions exist. Generally only one of these is the valid solution for the hand-directed sculpting tool pose. Through exhaustive simulation of the forward pose kinematics solution throughout the useful workspace, it was found that generally the positive y solution should be used in the three spheres intersection algorithm. However, an undesired result was sometimes found, illustrated in Figure 5.

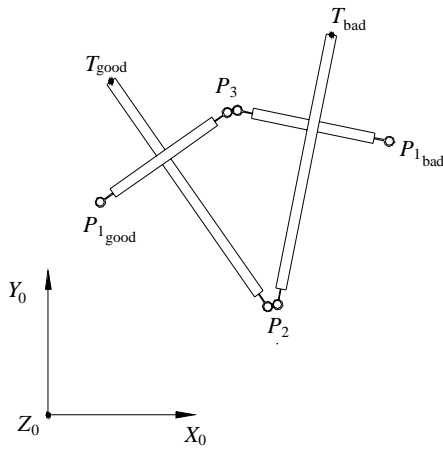


Figure 5. Multiple Solution Trouble

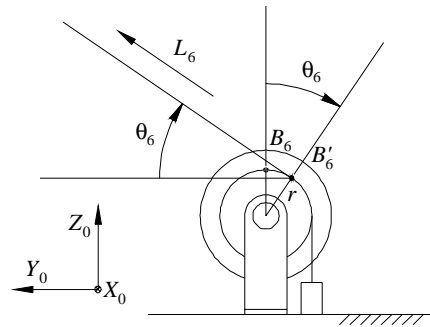


Figure 6. String Pot Pulley with Cable Angle

In Figure 5, the left part is the actual pose, while the right part is the erroneous pose. As seen in the figure, the solutions for P_2 and P_3 were as desired, but then point P_1 was flipped over as shown; this is impossible in the hardware as cables would be twisted unless they were disconnected and reattached in the undesired pose. To handle this type of problem in the forward pose kinematics solution, we write three inequalities, with respect to $\{0\}$, which must be satisfied for general operation of the tool:

$$P_{1x} < P_{3x} \qquad P_{2y} < P_{1y} \qquad P_{2y} < P_{3y} \qquad (24)$$

If the first inequality in x is not satisfied, we must use the negative y solution in the three spheres intersection algorithm when determining point P_1 (the third step).

However, for the second and third y inequalities in (24), the positive and negative y solutions yield identical results and hence cannot be used to distinguish the correct solution to use. Generally the positive y solution should be used in the three spheres intersection algorithm when determining points P_2 and P_3 (the first and second steps).

A second type of multiple solution case exists within the workspace, potentially more problematic than the easily-detected case given above. When the chainsaw is oriented so that P_2 and P_3 is in the workspace near AB , at many Z planes, it was observed that a second valid solution exists, with orientation much closer to the expected solution than the previous case of Figure 5. In this case, the expected solution can be found by using the positive y solution in the three spheres intersection algorithm when determining point P_1 , but using the negative y solution in the three spheres intersection algorithm for both P_2 and P_3 . The trick is in detecting when this occurs because both orientations are similar, unlike the flipped multiple solution case. This situation only occurs near the tetrahedral frame, which is to be avoided according to our singularity analysis.

3.2 Iterative Forward Pose Kinematics Solution

The preceding closed-form forward pose kinematics solution assumes that the ground-mounted fixed cable points C_1 , C_2 , C_3 , A_4 , A_5 , and B_6 are constant. However, as seen in Figure 6, these points change with cable angle θ_6 (shown for cable 6 in Figure 6: contact point B_6 moves to B'_6 due to cable/pulley angle θ_6). The closed-form solution assumed that all cables extend horizontally for A_4 , A_5 , B_6 and vertically for C_1 , C_2 , C_3 . That is, for instance, the point of contact was assumed to be the nominal B_6 rather than the actual B'_6 in Figure 6. Ignoring this issue leads to Cartesian position error norms of over 50 mm and Cartesian orientation error norms of over 2° in the worst cases (large cable angles). Therefore, this section discusses an iterative solution to reduce this error (see¹⁶ for more details). Each step of the iterative solution employs the closed-form solution from above.

The nominal horizontal and vertical cable cases are rare in actual operation; usually there is some cable angle as pictured in Figure 6. Note that the cable angle is always identical to the pulley angle. For a positive angle (shown as θ_6 ; positive is about X_0 into the page), the nominal point B_6 has moved to actual contact point B'_6 and the sensed cable length for the sixth cable is too short by $r\theta_6$ (the cable length error is $-r\theta_6$), where θ_6 is the cable/pulley angle ($r = 11.11 \text{ mm}$ (7/16")) for the contact pulley for all string pots). The cables are calibrated so that zero length is defined as when the cable tip is at point B_6 in Figure 6. Relative to nominal point B_6 , the new fixed cable point can be calculated using (25):

$${}^0\mathbf{B}'_6 = \begin{Bmatrix} B_{6x} \\ B_{6y} - r \sin \theta_6 \\ B_{6z} - r(1 - \cos \theta_6) \end{Bmatrix} \quad (25)$$

The same statements can be made for negative cable/pulley angles as well: for negative cable angles, going down in Figure 6, the new fixed point ${}^0\mathbf{B}'_6$ can still be calculated using (25) with $-\theta_6$, and this time the sensed cable

length for the sixth cable is too long by $r\theta_6$. Similar formulas apply to points $A_4, A_5, C_1, C_2,$ and C_3 , but different transformations are required for $\{0\}$ coordinates.

We assume that only the type of angle shown in Figure 6 is significant (up-and-down); the secondary angle (side-to-side) is generally smaller and will be ignored in this analysis. However, to calculate the up-and-down angle, we use the change in Z divided by the combined change in XY (below). So we ignore the side-to-side angle, but this motion affects the primary up-and-down angle. First, let us present formulas for calculating the six cable angles (θ_6 is shown in Figure 6 and required to calculate ${}^0\mathbf{B}'_6$ in (25); the remaining five angles are similarly defined and required). From geometry of each cable between the fixed and moving cable connection points:

$$\theta_i = \tan^{-1}\left(\frac{\Delta z_i}{\Delta xy_i}\right) \quad i = 4,5,6 \quad (26)$$

where:

$$\begin{aligned} \Delta z_4 &= P_{3z} - A_{4z} & \Delta xy_4 &= \sqrt{(P_{3x} - A_{4x})^2 + (P_{3y} - A_{4y})^2} \\ \Delta z_5 &= P_{2z} - A_{5z} & \Delta xy_5 &= \sqrt{(P_{2x} - A_{5x})^2 + (P_{2y} - A_{5y})^2} \\ \Delta z_6 &= P_{2z} - B_{6z} & \Delta xy_6 &= \sqrt{(P_{2x} - B_{6x})^2 + (P_{2y} - B_{6y})^2} \end{aligned}$$

$$\theta_i = \tan^{-1}\left(\frac{\Delta xy_i}{\Delta z_i}\right) \quad i = 1,2,3 \quad (27)$$

where:

$$\Delta z_i = C_{iz} - P_{iz} \quad \Delta xy_i = \sqrt{(P_{ix} - C_{ix})^2 + (P_{iy} - C_{iy})^2}$$

Note the signs of the angles will be determined automatically in (26), even using the plain *atan* function; these will be correctly determined by the sign of Δz_i . However, in (27), we forced Δz_i to be always positive; further, we use only the positive square root in Δxy_i , so we must determine the sign of the angles for $i=1,2,3$ by logic. Looking down the X_0 axis from the right of the machine, angles θ_i are positive when the tool tip places moving chainsaw point P_i forward of the vertical from fixed cable points C_i . The sign conditions are:

$$\begin{aligned} \theta_i \text{ is positive if} & \quad P_{iy} - C_{iy} > 0 \\ \theta_i \text{ is zero if} & \quad P_{iy} - C_{iy} = 0 \\ \theta_i \text{ is negative if} & \quad P_{iy} - C_{iy} < 0 \end{aligned} \quad i = 1,2,3 \quad (28)$$

All position vector components above are expressed in $\{0\}$ coordinates. Note there is some error in these formulas since we use the nominal fixed points to calculate all angles: we do not yet know the shifted fixed cable points. In the kinematics iterative solution to follow, we can update the angles based on the shifted cable points to reduce this error. Given the six cable angles, we can now present the formulas for the shifted fixed cable points (${}^0\mathbf{B}'_6$ was given in

(25)). The shifted fixed cable points for C_i are similar to ${}^0\mathbf{B}'_6$, but the nominal cable location is vertical and the points shift differently with respect to $\{0\}$:

$${}^0\mathbf{C}'_i = \begin{Bmatrix} C_{ix} \\ C_{iy} + r(1 - \cos \theta_i) \\ C_{iz} - r \sin \theta_i \end{Bmatrix} \quad i = 1, 2, 3 \quad (29)$$

The shifted fixed cable points for A_i are identical to ${}^0\mathbf{B}'_6$ in (25), but these are expressed in different coordinates, rotated by 120° about the Z_0 axis with respect to $\{0\}$, and with origins located on the nominal fixed cable points A_i . Thus, these formulas must be transformed to $\{0\}$ coordinates first as follows:

$${}^{A_i}\mathbf{A}'_i = \begin{Bmatrix} {}^{A_i}A_{ix} \\ {}^{A_i}A_{iy} - r \sin \theta_i \\ {}^{A_i}A_{iz} - r(1 - \cos \theta_i) \end{Bmatrix} \quad (30)$$

$${}^0\mathbf{A}'_i = {}^0\mathbf{T}_{A_i} {}^{A_i}\mathbf{A}'_i \quad (31)$$

where:

$${}^{A_i}\mathbf{A}_i = \begin{Bmatrix} {}^{A_i}A_{ix} \\ {}^{A_i}A_{iy} \\ {}^{A_i}A_{iz} \end{Bmatrix} = \begin{Bmatrix} 0 \\ 0 \\ 0 \end{Bmatrix}$$

$${}^0\mathbf{T}_{A_i} = \begin{bmatrix} \cos 120^\circ & -\sin 120^\circ & 0 & {}^0A_{ix} \\ \sin 120^\circ & \cos 120^\circ & 0 & {}^0A_{iy} \\ 0 & 0 & 1 & {}^0A_{iz} \\ 0 & 0 & 0 & 1 \end{bmatrix}$$

Since this cable/pulley angle error can be quite significant, we now develop an iterative forward pose kinematics solution incorporating the cable/pulley angles and shifted fixed cable points of (25-31). This solution must be iterative because, given the six sensed cable lengths, we first use the nominal fixed cable points to calculate the nominal Cartesian chainsaw pose (as in Section 3.1). But then we calculate the estimate for the six cable angles, which shifts the fixed cable points and modifies the cable lengths; we iterate until the Cartesian pose stops changing (according to a user-defined solution tolerance). This iterative forward pose kinematics solution is summarized below:

1. Given \mathbf{L}_{sensed} , the six cable lengths read from the string pots.
2. Calculate the closed-form forward pose kinematics solution as in Section 3.1.
3. Calculate the six cable/pulley angles and update the shifted fixed cable points (using (25-31)).
4. Modify the six cable lengths \mathbf{L}_{sensed} by $-r\theta_i$ on each cable i .
5. Repeat steps 2-4 until the change in Cartesian pose from the last step is sufficiently small.

Note it is important to always use the nominal fixed cable points in the shifted points formulas and to use the nominal \mathbf{L}_{sensed} at each step when calculating new cable lengths; otherwise the solution will run away. Upon implementation of this algorithm, it was discovered that only 3 to 5 iterations were required to reduce the translational and rotational error norms to 0.02 mm and 0.01° , respectively.

An alternate method to solve this problem is through mechanical design: each string pot can be fitted with a small plate with a small hole to guide each cable (in the nominal horizontal or vertical position) so that the ground-mounted fixed cable points never change. This would have the additional benefit of keeping all cables on their string pot pulleys at all times (it is not uncommon for one or more cables to slip off during normal motions) and reducing computation (no iteration required). However, the disadvantages of this mechanical solution are increased cable friction and wear and sharper cable angles.

4. RELATED KINEMATICS ISSUES

This section presents required kinematics issues for implementation and use of the six-cable sculpting metrology tool: Cartesian displacements for display to the operator, Cartesian measurement uncertainty given uncertainty in cable length measurements, calibration of the fixed cable points, and system workspaces.

4.1 Displacements for Display

This section presents equations for displaying displacement errors to the human sculptor from the hand-directed sculpting tool. Presented is the difference (error) between the target pose for the chainsaw and the current pose of the chainsaw. That is, assume a target pose (or a trajectory of target poses) is given for the sculpting tool. Let the target pose be represented by coordinate frame $\{TARG\}$ and let the current chainsaw pose be represented by $\{T\}$. The sculptor's goal is to drive $\{T\}$ towards $\{TARG\}$ at all times, to execute the desired piece from a computer model.

The pose displacement errors between the target and current poses are derived for display to the operator as follows. It is easy for translations, and less straight-forward for rotations. For translation errors, the position error vector ${}^0\mathbf{P}_E$ is found by vector subtraction:

$${}^0\mathbf{P}_E = \begin{Bmatrix} x_E \\ y_E \\ z_E \end{Bmatrix} = \begin{Bmatrix} {}^0x_{TARG} - {}^0x_T \\ {}^0y_{TARG} - {}^0y_T \\ {}^0z_{TARG} - {}^0z_T \end{Bmatrix} \quad (32)$$

The result ${}^0\mathbf{P}_E$ gives the XYZ displacements to translate the tool tip along, in the world coordinates, to drive $\{T\}$ towards $\{TARG\}$.

Unfortunately, no description of orientation is a vector description. That is, we cannot simply subtract the target and current Euler angles (or fixed angles), analogously to the translation difference (32). Instead, we can use the rotation matrix form to determine a difference (error) rotation matrix, and extract the error $\mathbf{Z-Y-X}$ ($\alpha-\beta-\gamma$) Euler angles (identical to the error $\mathbf{X-Y-Z}$ ($\gamma-\beta-\alpha$) fixed angles¹²) from the difference rotation matrix. The difference rotation matrix is ${}_{TARG}^T\mathbf{R}$, expressing the orientation of $\{TARG\}$ with respect to the current pose $\{T\}$:

$${}_{TARG}^T\mathbf{R} = [{}^T_0\mathbf{R}] [{}^0_{TARG}\mathbf{R}] = [{}^0_T\mathbf{R}^{-1}] [{}^0_{TARG}\mathbf{R}] = [{}^0_T\mathbf{R}^T] [{}^0_{TARG}\mathbf{R}] \quad (33)$$

In (33) we take advantage of the beautiful property that $R^{-1} = R^T$ for orthonormal rotation matrices¹². Now we extract the error Euler angles (or fixed angles) from $\begin{bmatrix} T \\ TARG \end{bmatrix} \mathbf{R}$ and display these to the operator. The result $\alpha_E, \beta_E, \gamma_E$ gives the **Z-Y-X** Euler rotational displacements to rotate the tool orientation about, with respect to world coordinates, to drive $\{T\}$ towards $\{TARG\}$. Note due to the definition of Euler angles, we must reverse the rotation order and do the γ about X_T rotation first, followed by β rotation about Y_T and then α rotation about Z_T . We cannot do the rotations in any order as we can do for translations. In the case of fixed angles, we would first do the α rotation about Z_0 , followed by β rotation about Y_0 and then γ about X_0 , again reverse the original definition, to drive $\{T\}$ toward $\{TARG\}$.

The Cartesian displacement error formulas developed in this section should be displayed to the operator so that the human can drive all tool-tip errors to zero for all sculpted poses. This subsection derived the formulas with respect to the world frame; in practice, a relative mode will be used as often as the world mode. That is, the chainsaw frame $\{T\}$ will be touched to the sculpture material in three or more reference poses (called poses $\{m_i\}$, $i = 1, 2, 3, \dots$); this will align the real world with the same reference poses in the computer model. Sculpting motions will then be made relative to one or more of these reference poses, rather than the world frame. Similar error formulas apply: simply replace index 0 with the desired reference pose m_i in (32) and (33).

4.2 Cartesian Uncertainty

This section presents simulated Cartesian pose measurement uncertainty errors $\Delta \mathbf{X}$ given a δ uncertainty in cable length measurements from the string pots. This section establishes a baseline regarding the sculpting tool resolution for aiding a sculptor in generating a carving. This resolution varies with the nominal Cartesian pose.

We apply a forward pose kinematics method for determining Cartesian uncertainty, applied to a grid of nominal poses (vertices of cubes of 0.5 m side, centered about the origin of $\{0\}$, for Z planes 0.25, 0.75, 1.25, and 1.75 m, for ‘all orientations’, see below). About each nominal pose \mathbf{X}_{nom} (we first use inverse pose kinematics to determine the nominal set of cable lengths \mathbf{L}_{nom}), we form all possible permutations $L_{nom_i} \pm \delta/2$, $i = 1, 2, \dots, 6$. For each of these $2^6=64$ permutations, we use forward pose kinematics to calculate \mathbf{X}_{err} , the uncertain Cartesian pose in each case. For each case we calculate the Cartesian error:

$$\Delta \mathbf{X} = \mathbf{X}_{err} - \mathbf{X}_{nom} \quad (34)$$

where $\Delta \mathbf{X} = \{\delta x \quad \delta y \quad \delta z \quad \delta \alpha \quad \delta \beta \quad \delta \gamma\}^T$ is the vector of Cartesian pose measurement uncertainty errors. For all 64 permutations, we average all Cartesian error components separately; note we must use absolute value for all error components or the resulting average Cartesian uncertainty would always be zero. Then we calculate the translational and rotational norms of the average Cartesian errors:

$$\|e_T\| = \sqrt{\delta x_{avg}^2 + \delta y_{avg}^2 + \delta z_{avg}^2} \quad \|e_R\| = \sqrt{\delta \alpha_{avg}^2 + \delta \beta_{avg}^2 + \delta \gamma_{avg}^2} \quad (35)$$

The error norms $\|e_T\|$ and $\|e_R\|$ represent the Cartesian pose measurement uncertainty errors. These measures are the length of the 3D diagonals of rectangular parallelepipeds bounded by $\delta x_{avg}, \delta y_{avg}, \delta z_{avg}$ and $\delta \alpha_{avg}, \delta \beta_{avg}, \delta \gamma_{avg}$, the distance between the uncertain average and nominal Cartesian poses. We wish these metrics to be as small as possible given a specific δ , for a high-resolution machine.

As mentioned above, we consider ‘all possible orientations’: at each tool tip grid point, let us consider all Euler angles $\alpha = \pm 45^\circ$, $\beta = \pm 45^\circ$, $\gamma = \pm 45^\circ$ in all possible permutations with an angle step size of 15° . We have $7^3=343$ possible orientations at each tool tip point. For each point, among the 343 orientations, we will report the average values over all orientations of the average $\|e_T\|$ and $\|e_R\|$ over all forward pose kinematics permutations. Now, many of these orientation combinations are outside the workspace, due to cable length limits; we skipped these conditions in the data presented below.

The grid described above is given in XY coordinates in Table I. The average Cartesian pose measurement uncertainty error data for the grid of tool-tip points and ‘all possible orientations’ are presented in Tables II-V, in the same arrangement as Table I for each Z plane. From laboratory observations the cable measurement uncertainty resolution is $\delta = 0.05 \text{ mm}$. Note the equilateral triangle ABD in Figure 1 has sides of length 3.048 m (120 inches). The units of translational error norms are mm and $degrees$ for rotational error norms in Tables II-V.

Table I. Grid of X,Y Tool-Tip Points (m) for each Z Plane

-0.5,0.5	0,0.5	0.5,0.5
-0.5,0	0,0	0.5,0
-0.5,-0.5	0,-0.5	0.5,-0.5

With $\delta = 0.05 \text{ mm}$, an important value for the translational error norm is $\|e_T\| = \sqrt{3(0.05)^2} = 0.0866 \text{ mm}$; at this value, the Cartesian error is equivalent to δ on each of $\delta x, \delta y, \delta z$ (of course the components can shift up and down to still yield 0.0866 mm). A smaller error means the machine reduces the effect of δ and a larger error means the effects of δ are amplified at the given pose. The units of $\|e_R\|$ have been converted to $degrees$ for the results tables below.

Table II. (Z=0.25 m) Translational Errors (mm)

0.07	0.07	0.08
0.07	0.12	0.20
0.08	0.20	0.57

Rotational Errors ($^\circ$)

0.01	0.01	0.01
0.01	0.01	0.01
0.01	0.01	0.03

Table III. (Z=0.75 m) Translational Errors (mm)

0.07	0.07	0.08
0.08	0.16	0.33
0.08	0.38	0.42

Rotational Errors ($^\circ$)

0.01	0.01	0.01
0.01	0.01	0.02
0.01	0.02	0.02

Table IV. ($Z=1.25\text{ m}$) Translational Errors (mm)

0.07	0.07	0.11
0.08	0.21	0.39
0.11	0.41	0.45

Rotational Errors ($^{\circ}$)

0.01	0.01	0.01
0.01	0.01	0.03
0.01	0.03	0.03

Table V. ($Z=1.75\text{ m}$) Translational Errors (mm)

0.07	0.08	0.24
0.09	0.34	0.61
0.39	0.36	0.27

Rotational Errors ($^{\circ}$)

0.01	0.01	0.02
0.01	0.02	0.04
0.02	0.03	0.02

From the Cartesian uncertainty error norms of Tables II-V, for a given Z plane, most errors decrease to the front and to the left in the workspace. This is due to longer cables yielding lower relative errors, for the same δ . For Tables II-IV the largest error is in the lower right corner, for both translations and rotations; this point approaches a singularity where two cables nearly become collinear. The machine will be unreliable near singularities in terms of Cartesian uncertainties given finite cable length measurement uncertainties. In order to avoid algorithmic singularities in forward pose kinematics, the moving cable connection points must stay away from the boundaries of the ground truss defined by points A , B , and C . In Table V, this singularity has moved nearer the (2,3) and (3,2) locations.

Tables II-V all have elements where the average translational error norm is less than 0.0866 mm . Translational errors under this value are good since this means that the cable sculpting tool is diminishing the effects of cable measurement uncertainty δ in these regions. All poses where the normalized translational error is greater than 0.0866 mm amplify the effects of cable measurement uncertainty δ .

Generally all rotational errors given in Tables II-V are very low (all rotational units are *degrees*). Due to the relatively long rotational arms on the chainsaw between moving points P_1 , P_2 , and P_3 , and T , the rotational error is diminished compared to the translational error. All errors are in the hundredths of *degree* range. The worst rotational error is 0.04° , which combines all three rotational axes. It appears that rotational errors will not cause any problem in the sculpting tool. The translational errors dominate; the worst of these is only 0.61 mm .

Since the above grid of poses was central to the reachable workspace, we also checked the Cartesian uncertainties at various outlying points, on the boundary of the reachable workspaces; we did not find higher errors for these cases. Also, the above results are for the specific δ of 0.05 mm observed in the system; though the forward pose kinematics problem is non-linear, we found that doubling δ to 0.10 mm roughly doubled all error norms in Tables II-V.

For the 0.05 mm δ value, our results show that the Cartesian resolution varies between 0.07 and 0.61 mm for translations and between 0.01° and 0.04° for rotations (both measures are combined for the three XYZ axes). These Cartesian uncertainty values are very small considering the large scale of the sculpting problem. According to sculptor Helaman Ferguson, a Cartesian resolution of 1 cm is sufficient for large sculpting projects. This subsection shows that all translational Cartesian uncertainties are far below this 1 cm level. Since the system is a hand-directed metrology

system driven by a human, a much more significant source of problems is tremors and errors from the human hands. The chainsaw further is very heavy; thus a gravity offload system will help the human maintain desired resolution; the metrology system resolution is more than that required.

4.3 Calibration of Fixed Cable Points

What if the locations of the fixed cable points $A_4, A_5, B_6, C_1, C_2,$ and C_3 are not known precisely? This section presents a method for calibration of these points given length readings from three known poses within the workspace. That is, touching the tool tip to a known XYZ position, plus a known orientation, we read the six cable lengths via the string pots. This is performed for three distinct poses ${}^0_{T_1}\mathbf{T}$, ${}^0_{T_2}\mathbf{T}$, and ${}^0_{T_3}\mathbf{T}$, and the following mathematics calculates the vector positions of fixed cable connection points $A_4, A_5, B_6, C_1, C_2,$ and C_3 . The first step in the solution process is to determine the chainsaw cable attachment points $P_1, P_2,$ and P_3 , one set for each given (touched) pose:

$$\begin{bmatrix} {}^0_{P_{ij}}\mathbf{T} \end{bmatrix} = \begin{bmatrix} {}^0_{T_j}\mathbf{T} \end{bmatrix} \begin{bmatrix} P_{ij} \end{bmatrix} \mathbf{T}^{-1} \quad i = 1,2,3 \quad j = 1,2,3 \quad (36)$$

In this subsection, point P_{ij} is defined as:

$${}^0\mathbf{P}_{ij} = \begin{Bmatrix} P_{ijx} \\ P_{ijy} \\ P_{ijz} \end{Bmatrix} \quad (37)$$

where ${}^0\mathbf{P}_{ij}$ is the position vector to moving cable connection point P_i , for the j^{th} given pose ($i = 1,2,3$ and $j = 1,2,3$).

${}^0\mathbf{P}_{ij}$ is extracted as the last column, first three rows, of (36).

To solve this overall calibration problem, let us first consider only cable 4, which connects fixed point A_4 (unknown) to moving point P_3 (known in three poses from (36)), via length L_4 (known in the three poses from the fourth string pot). The key to the problem is to recognize that A_4 is the intersection of three spheres, whose centers are the three known points P_{3j} and whose radii are the three sensed values L_{4j} , $j = 1,2,3$. Note we define L_{ij} as the sensed length for cable i , in the j^{th} given pose ($i = 1,2,\dots,6$ and $j = 1,2,3$). The equations for these three spheres are:

$$\begin{aligned} (A_{4x} - P_{31x})^2 + (A_{4y} - P_{31y})^2 + (A_{4z} - P_{31z})^2 &= L_{41}^2 \\ (A_{4x} - P_{32x})^2 + (A_{4y} - P_{32y})^2 + (A_{4z} - P_{32z})^2 &= L_{42}^2 \\ (A_{4x} - P_{33x})^2 + (A_{4y} - P_{33y})^2 + (A_{4z} - P_{33z})^2 &= L_{43}^2 \end{aligned} \quad (38)$$

The unknown point A_4 may easily be found using the Intersection of Three Spheres algorithm developed earlier for Forward Pose Kinematics. This algorithm appears in (4-15).

To finish the calibration of fixed cable points $A_4, A_5, B_6, C_1, C_2,$ and C_3 , simply apply the three spheres intersection algorithm six times (including the case described above), as follows:

1. C_1 is the intersection of: $({}^0\mathbf{P}_{11}, L_{11}), ({}^0\mathbf{P}_{12}, L_{12}), ({}^0\mathbf{P}_{13}, L_{13})$
2. C_2 is the intersection of: $({}^0\mathbf{P}_{21}, L_{21}), ({}^0\mathbf{P}_{22}, L_{22}), ({}^0\mathbf{P}_{23}, L_{23})$

3. C_3 is the intersection of: $({}^0\mathbf{P}_{31}, L_{31}), ({}^0\mathbf{P}_{32}, L_{32}), ({}^0\mathbf{P}_{33}, L_{33})$
4. A_4 is the intersection of: $({}^0\mathbf{P}_{31}, L_{41}), ({}^0\mathbf{P}_{32}, L_{42}), ({}^0\mathbf{P}_{33}, L_{43})$
5. A_5 is the intersection of: $({}^0\mathbf{P}_{21}, L_{51}), ({}^0\mathbf{P}_{22}, L_{52}), ({}^0\mathbf{P}_{23}, L_{53})$
6. B_6 is the intersection of: $({}^0\mathbf{P}_{21}, L_{61}), ({}^0\mathbf{P}_{22}, L_{62}), ({}^0\mathbf{P}_{23}, L_{63})$

Note in each case, the spheres' intersection is found from the same moving cable connection point and the same cable, but for three different known poses and measured lengths. Now, since we use the same sphere intersection algorithm from forward pose kinematics, this fixed cable points calibration is subject to the same imaginary solutions, multiple solutions, and algorithmic singularities problems. If imaginary solutions result, this means one or more spheres do not intersect; this means there is a modeling or sensing error. The multiple solutions will cause no trouble, since approximate values for the fixed cable points are known. Further, if a different Z value is chosen for each of the known poses, and if the known orientations are kept to nominal (i.e. $\alpha = \beta = \gamma = 0$), none of the algorithmic singularities will be a problem.

The methods in this subsection will work well only if the fixed cable points are truly fixed (see Section 3.2 and Figure 6). Otherwise, there will be some error due to the cable/pulley angles shifting the cable contact points. Thus, fixed point calibration is another reason to add a plate with a fixed hole to each of the string pots. If this mechanical guide is not added, an iterative procedure similar to Section 3.2 may be implemented to reduce this error in the fixed cable point calibration due to cable/pulley angles.

4.4 Workspaces

The workspace is defined as the 3D volume that is attainable by the tip $\{T\}$ of the six-cable hand-directed sculpting metrology tool, both in position and orientation. We are interested in three types of workspace: reachable, zero-orientation, and dexterous. The reachable workspace is the 3D volume reachable by the tool tip regardless of orientation; if a point is reachable in only one specific orientation, it is considered part of the reachable workspace. The zero-orientation workspace is that 3D volume that can be reached by the tool tip with the constraint of nominal orientation only, $\alpha = \beta = \gamma = 0$. The dexterous workspace is that 3D volume reachable by the tool tip in all possible orientations. For most parallel robots, the dexterous workspace vanishes, so we must define a limit on dexterous workspace, such as $\pm 30^\circ$ on α , β , and γ . Generally, the zero-orientation workspace is a subset of the reachable workspace, and the dexterous workspace is a subset of the zero-orientation workspace.

The workspaces are limited by the 2.54 m (100 inch) string pot cable excursions. For the hardware, the length constraints are $1.778 \leq L_i \leq 4.318$ m ($70 \leq L_i \leq 170$ inches) for $i = 1, 2, 3$ and $0 \leq L_i \leq 2.54$ m ($0 \leq L_i \leq 100$ inches) for $i = 4, 5, 6$. Note we added cable extensions of 1.778 m (70 inches) to cables 1, 2, and 3 to bring the tool to normal heights for sculptors standing on the floor. We have developed a geometric workspace determination method for certain

planes¹⁶. However, in this section we use a numerical computer method to determine the 3D reachable, zero-orientation, and $\pm 30^\circ$ dexterous workspaces.

In the numerical workspace results presented below, we discretized the possible pose space as follows. We search over all pertinent XY points with $\Delta_x = \Delta_y = 0.05$ m. For the reachable and dexterous workspaces, we vary α, β, γ over all possible permutations in the ranges $\pm 30^\circ$, with $\Delta_\alpha = \Delta_\beta = \Delta_\gamma = 10^\circ$. All Z planes have the same XY plane limits in the workspace plots below; the ABD equilateral frame is shown for reference in each. We consider nine Z planes, evenly spaced within the workspace; the workspace plots below follow the Z -plane arrangement shown in Table VI (m):

Table VI. Z-planes (m) for Numerical Workspace Determination

0	0.4	0.8
1.2	1.6	2.0
2.4	2.8	3.2

Figures 7a-c present the numerical reachable, zero-orientation, and $\pm 30^\circ$ dexterous workspaces, respectively, for the hand-directed sculpting tool. These show the theoretical workspace extents; the useful workspaces are bounded by the planes of the tetrahedral frame. The dexterous workspace is dependent on the limited angle ranges chosen. For instance, the $\pm 45^\circ$ dexterous workspace (not shown) is nearly void; in that case, there is a small workarea on Z planes 0.8, 1.2, and 1.6; the remaining Z planes are completely blank.

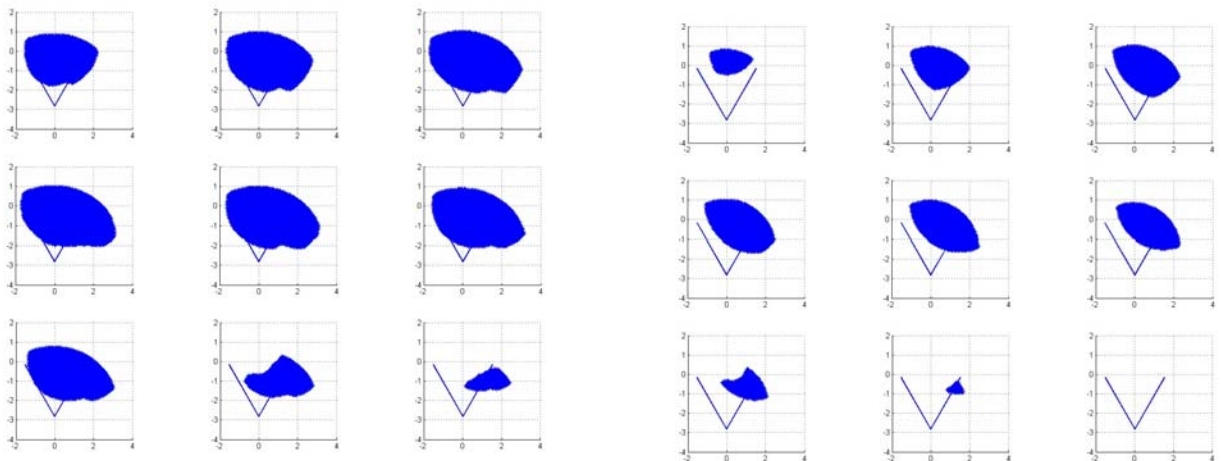


Figure 7a. Numerical Reachable Workspace **Figure 7b. Numerical Zero-Orientation Workspace**

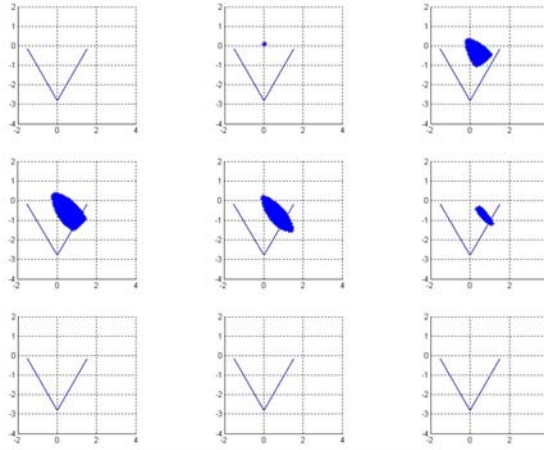


Figure 7c. Numerical Dexterous Workspace

The axis units in Figures 7a-c are m (the equilateral triangle ‘V’ shown has sides of length $3.048 m$). The X_0 limits are -2 to $4 m$ and the Y_0 limits are -4 to $2 m$ for all subplots in Figures 7. This concludes our presentation of workspace. For more details on workspace, plus all topics in Sections 3 and 4, including simulation examples for all of the related kinematics problems, please see¹⁶.

5. EXPERIMENTAL RESULTS

This section presents experimental results from the NIST cable-based metrology system. Three experiments are presented, typical of the many diverse motions we have tested in the lab: an absolute, combined-axis translational motion, an absolute rotation about a single Cartesian axis, plus relative surface motions on a torus. We present experimental data and compare it to simulated motions. We also present a discussion of absolute accuracy, measurement resolution, and errors, plus ideas for design improvements.

The six identical string pots in our system are ten-turn potentiometers allowing a length change of $2.54 m$ ($100 inches$). The nylon-coated, $0.5 mm$ diameter, twisted stainless steel cable winds around the internal potentiometer drum in a single layer (thus, no error due to the cable winding onto itself). The manufacturer states the temperature range as -40 to $200 ^\circ C$ and the temperature-dependent cable elongation as $158 \times 10^{-6} / ^\circ C$. A torsional spring maintains tension (about $2 N$) on each cable at all times; we have developed a method to calculate the load the human exerts to overcome the cables’ tension for any Cartesian motion, but this is not significant and hence not presented (in some cases the cable tensions help rather than hinder the specific motion). The experimental results in this section were obtained using a light proxy cross for the sculptor’s chainsaw; for the production model we are designing a gravity-offload assist mechanism for unloading the human as much as possible. The six string pot potentiometer voltage readings are sent to the PC via an external interface box and an internal PCI DAQ (data acquisition) card. LabView* software is used for the metrology system, with Matlab* calculating the Cartesian pose for LabView* at each cycle, running at $10 Hz$.

* The identification of any commercial product or trade name does not imply endorsement or recommendation by Ohio University or NIST.

5.1 Experiment 1: Absolute, Combined-Axis Translational Motion

The first experiment involved a straight-line translational motion in the combined X_0Y_0 absolute directions. A heavy Aluminum straight edge was aligned by $\alpha = -30^\circ$ about Z_0 on a lab table just over 1 m high. The human guided the tool tip along this edge on the table top, attempting to maintain the initial orientation. The commanded initial and final poses for this case were:

$$\mathbf{X}_i = \{-0.0429 \quad 0.5588 \quad 1.0160 \quad -30 \quad 0 \quad 0\} \quad \mathbf{X}_f = \{0.6170 \quad 0.1778 \quad 1.0160 \quad -30 \quad 0 \quad 0\}$$

The experimental (solid) and simulated (dashed) cable lengths are plotted below for motion along the straight X_0Y_0 line in Figure 8a, followed by the experimental (solid) and simulated (dashed) absolute Cartesian pose variables in Figure 8b. Figure 8c presents the same X_0Y_0 data as that of Figure 8b, but plotted Y_0 vs. X_0 rather than vs. *time*. The absolute x error of 32 mm is evident at the end of motion in the X_0Y_0 plane. Figure 8c shows the desired and measured straight line in Cartesian space. Figure 8d shows the experimental environment for this case.

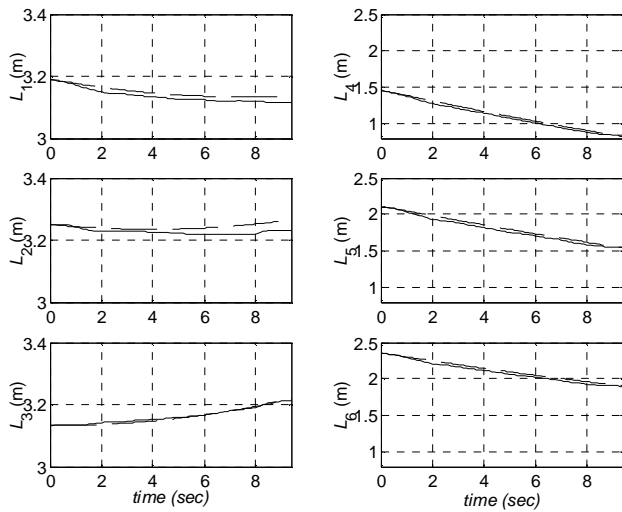


Figure 8a. Cable Lengths, XY Motion

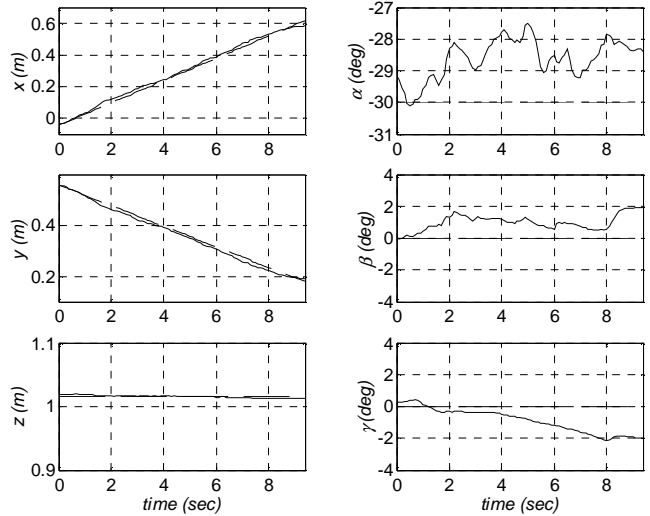


Figure 8b. Cartesian Pose, XY Motion

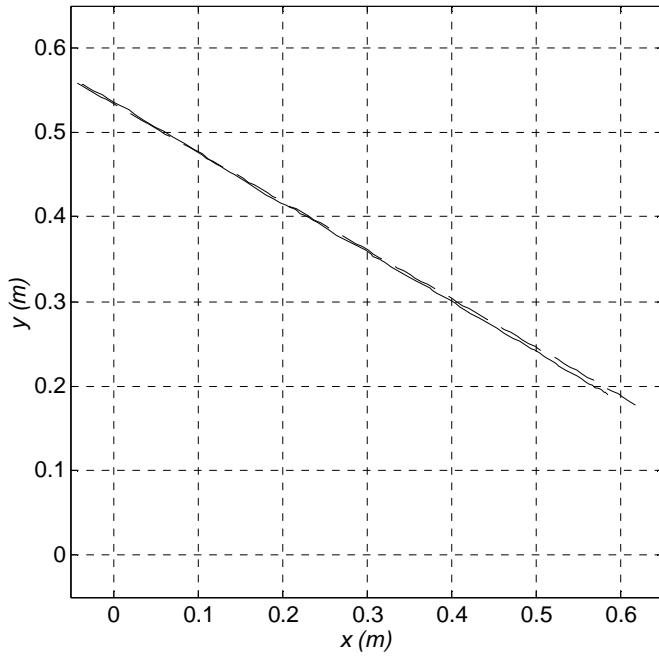


Figure 8c. Absolute Cartesian Pose, X_0Y_0 Motion



Figure 8d. Lab Table, X_0Y_0 Motion

The agreement is good as seen in the above plots. We can see significant human error during motion, especially in cables 1 and 2 (it appears that these cables dwell during motion due to human inputs, where they should change continuously and smoothly as shown in the dashed lines), plus all three Cartesian Euler angles. The average α angle seems to be off by 1° , but this could be due to workspace placement of the straight line or human motion error as much as metrology system error. Since it is difficult to read in the above scale, the worst absolute error magnitudes for this motion are given in the table below, for each axis, absolute values (*mm* and *degrees*); these values are the maximum error at the start or end since significant human errors may occur in between.

Table VII. Absolute Errors, X_0Y_0 Translational Motion

	x (mm)	y (mm)	z (mm)	α ($^\circ$)	β ($^\circ$)	γ ($^\circ$)
Maximum Absolute Error	32	12	4	1.6	1.9	2.0

The errors may be decreased by implementing a relative mode, wherein subsequent poses are measured with respect to a defined reference pose(s). Errors decrease because the uncertainty of the absolute reference to the world frame is removed. Also, as we will discuss later, much of the error is due to imperfect human-guided motions and workspace measurements, rather than the metrology system itself.

5.2 Experiment 2: Absolute, Single-Axis Rotational Motion

The second experiment involved a single-axis rotation, α , about the absolute Z_0 axis. The tool tip was supported on the lab tabletop, over 1 m high. Taking care not to change the translational location of the tool tip, the human rotated the tool about its tip, also attempting to maintain nominal zero orientation for β and γ . The commanded initial and final poses for this case were:

$$\mathbf{X}_i = \{-0.0302 \quad 0.1778 \quad 1.0160 \quad 0 \quad 0 \quad 0\} \quad \mathbf{X}_f = \{-0.0302 \quad 0.1778 \quad 1.0160 \quad 45 \quad 0 \quad 0\}$$

The experimental (solid) and simulated (dashed) cable lengths are plotted in Figure 9a for rotation about Z_0 , followed by the experimental (solid) and simulated (dashed) Cartesian pose variables in Figure 9b.

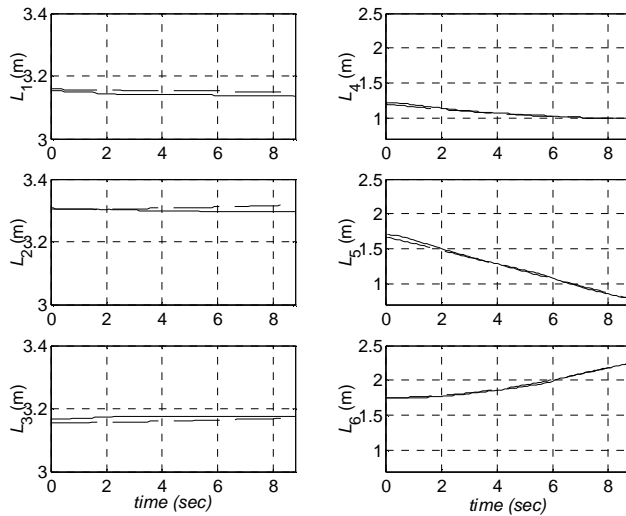


Figure 9a. Cable Lengths, α Motion

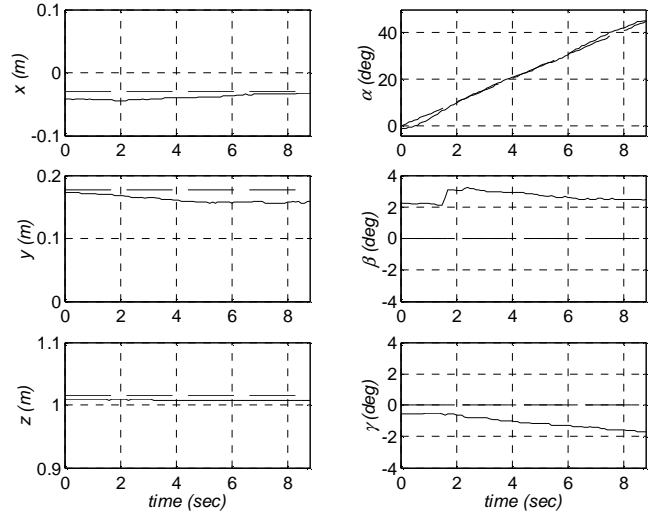


Figure 9b. Cartesian Pose, α Motion

The agreement is good as seen in the above plots. We can see significant human error during motion, especially in maintaining fixed tool tip position. Since it is difficult to read in the above scale, the worst absolute error magnitudes for this motion are given in the table below, for each axis, absolute values (*mm* and *degrees*); these values are the maximum error at the start or end since significant human errors may occur in between.

Table VIII. Absolute Errors, α Rotational Motion

α Rotation	x (mm)	y (mm)	z (mm)	α ($^\circ$)	β ($^\circ$)	γ ($^\circ$)
Maximum Absolute Error	12	19	8	1.1	2.5	1.7

Again, the errors may be decreased using relative mode, and much of the error is due to human-guided motions and workspace measurements, rather than the metrology system itself.

5.3 Experiment 3: Relative Torus Surface Motions

Experiment 3 involved tracing the surface of a torus model (see Figure 10a, made of Styrofoam, whereas the real-world material would be granite) with the tool tip (Figure 10b). We have two sub-experiments, tracing the larger, outer diameter in the XY plane and also tracing the smaller, cross sectional circle diameter in the YZ plane; the torus is placed on the lab tabletop for both. For both sub-experiments, the tool is kept radial to the appropriate circle at all times, so that only one Euler angle varies (α and γ , respectively); the remaining angles are kept to nominal and the other translations are kept in the respective planes of motion. In both cases, the relative translational measurement results (Figures 11a and 12a) are given relative to a reference point defined in each case to be the center of the circle of interest. This removes the absolute frame world uncertainty (the above descriptions are for attempted motion relative to the torus, not the world frame). In Figures 11a and 12 a, the dashed lines show the edges of the torus, while the solid lines show the measured data. Figures 11b and 12 b show the associated relative Euler angles measured during these torus experiments.



Figure 10a. Styrofoam Torus

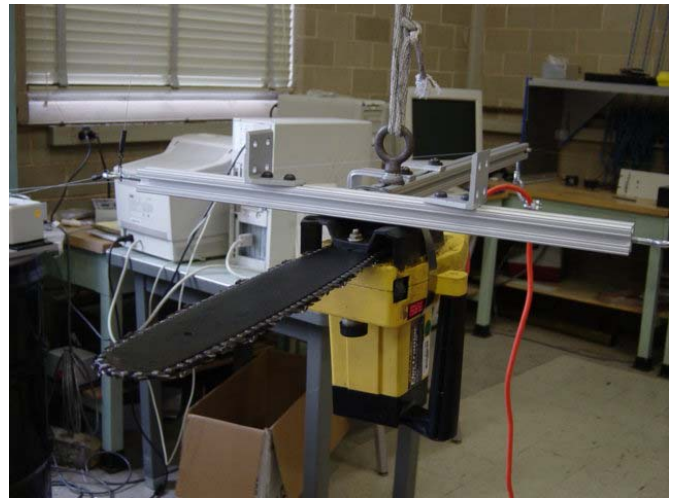


Figure 10b. Chainsaw

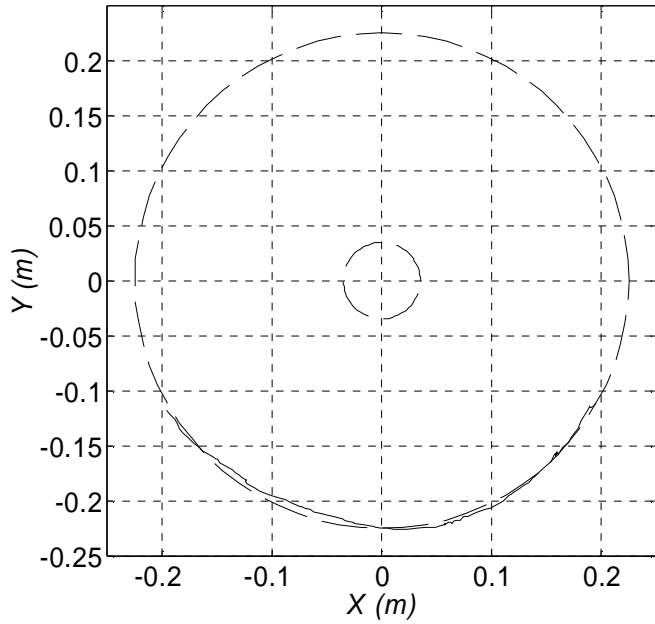


Figure 11a. XY Relative Torus Measurement

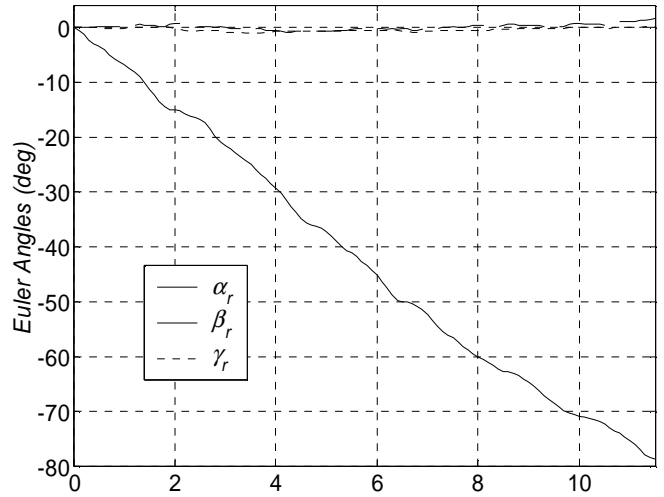


Figure 11b. Associated Relative Euler Angles

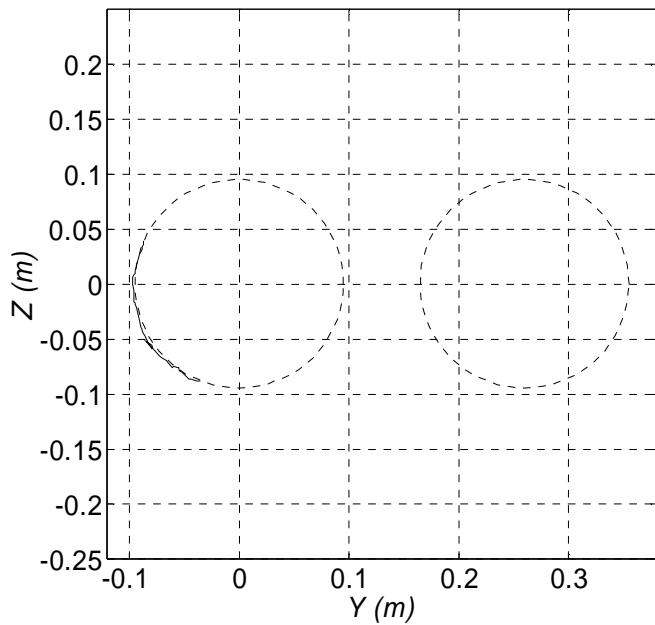


Figure 12a. YZ Relative Torus Measurement

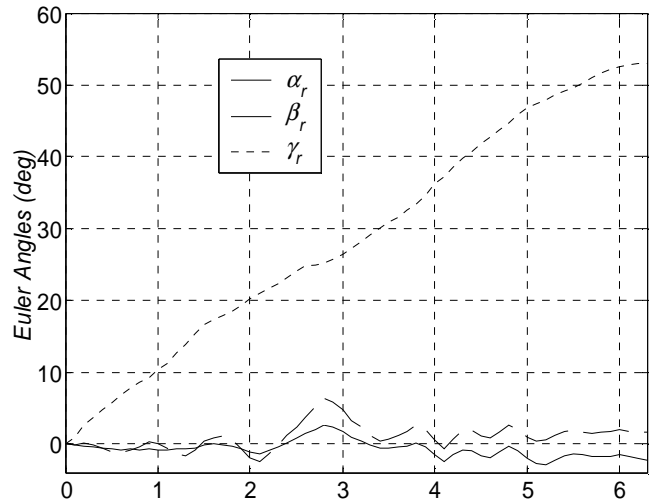


Figure 12b. Associated Relative Euler Angles

In the experiment of Figures 11, the human guided the tool tip from right to left, radially along the torus surface as shown; not quite one-fourth of the torus was traversed since the Euler angle α starts from its initial value (defined in the relative mode to be zero) and rotates in the negative direction about the Z axis to around -80° . In the experiment of Figures 12, the human guided the tool tip from up to down, radially along the torus surface as shown; not quite one-sixth of the torus was traversed in this case since the Euler angle γ starts from its initial value and rotates in the positive direction about the X axis to nearly 60° .

The metrology system displays in real-time (at a rate of 10 Hz) to the human operator: the six potentiometer voltages, the six calibrated cable lengths, and the Cartesian pose (three vector position components and three Euler angles). The Cartesian pose can be displayed either absolute, with reference to the world frame {0}, or relative, with reference to one or more poses defined by touching the tool tip to the material under development or other items in the workspace. Figure 13 shows another type of real-time visual feedback from the metrology system to the operator. This figure shows the four views (isometric and three planar projections) of the virtual CAD model for the 3D surface to be sculpted (in this case, a torus); this can be defined in an absolute or relative mode (relative mode seems to be more useful in the lab). A relative mode is used in Figure 13, where the reference point is an asterisk shown on the torus surface (at [0 0 0]), with associated desired orientation (three mutually-orthogonal lines whose origin is the asterisk), in this case lined up with the XYZ axes shown. The floating pose shown is the actual tool-tip location, which updates (in position and orientation) every tenth of a second. A representation of a diamond-tipped chainsaw blade is shown in all views. The operator can move the tool-tip until it coincides with the target pose, in this case the reference pose shown on the torus. The system gives the operator the relative difference between target and current poses (three relative vector position components and three relative Euler angles) to aid in reaching the desired pose.

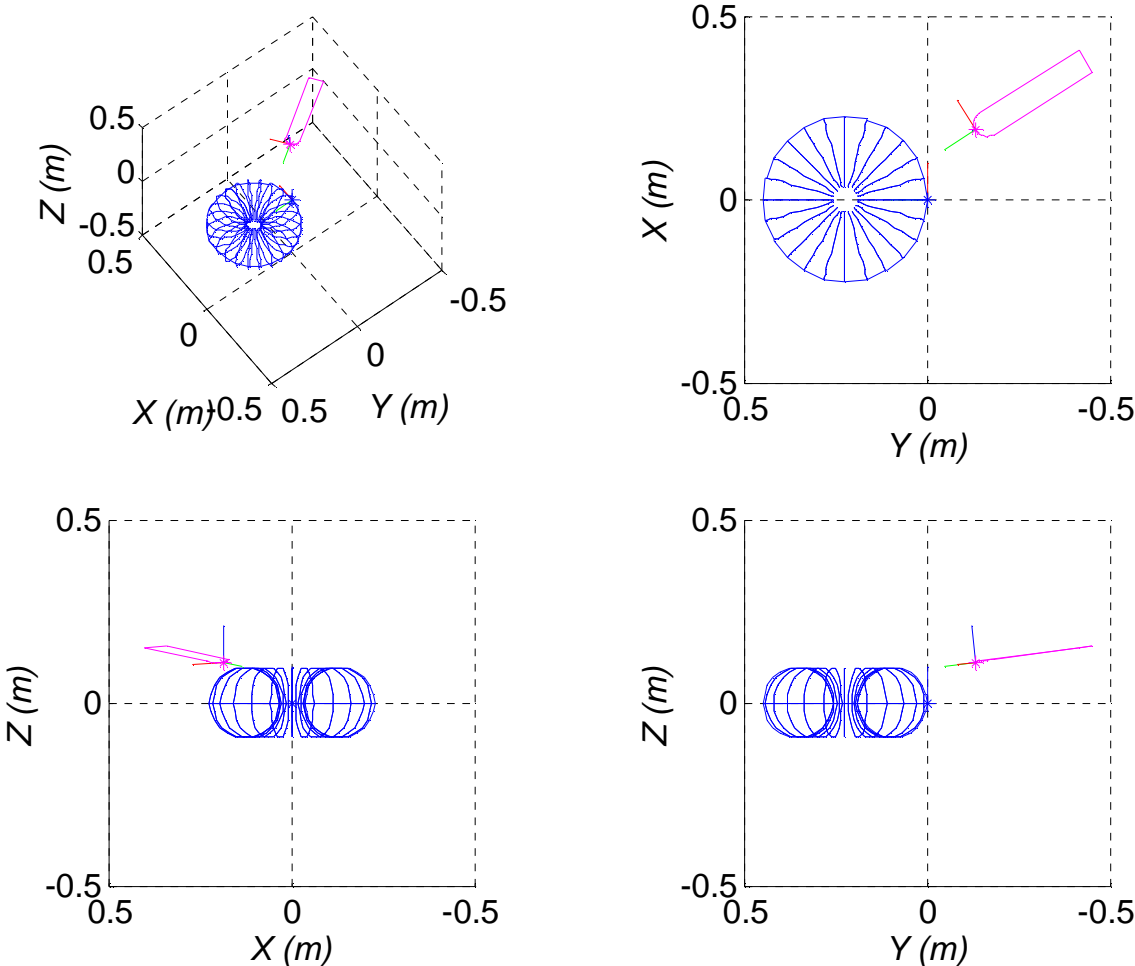


Figure 13. Virtual Surface with Pose Updated in Real-Time

5.4 Experimental Error Discussion

This subsection enumerates and discusses the various error sources in laboratory experiments concerning the above results. The potential error sources are many, as given in the following list.

- Cable/pulley errors as discussed in Section 3.2. The results presented do not use the iterative forward pose kinematics solution; however, when we did apply this iterative solution to check the effect on errors, nearly all cases were basically indistinguishable. The iterative procedure required 2-4 iterations at each step to achieve translational and rotational error tolerances to 0.02 mm and 0.01° , respectively. So, this source of error can be significant as discussed in Section 3.2; however, the experiments measured motions largely staying near the central plane containing points A_4 , A_5 , and B_6 and thus this type of error is small in our results.
- In the hardware chainsaw proxy, the current design allows points P_1 , P_2 , and P_3 to slide significantly around a 2.54 cm (1 in) eyebolt. We tried to manage this during data collection, but it should be improved in design.
- We cannot know exact values for the fixed cable connection points A_4 , A_5 , B_6 , C_1 , C_2 , C_3 ; Section 4 presents an on-line method which may help, but there will always be some error here.
- It is difficult to measure precise Cartesian positions and orientations in the workspace of the metrology system; such values are used as the perfect measure that the experimental data is compared with.
- In a related vein, we do not know the precise location and orientation of the lab bench in the metrology system workspace that was so central to generating straight lines and single-axis rotations. We assumed it was perfectly aligned in the XYZ directions of $\{0\}$ and also that the various edges were perfectly straight. This assumption is reasonable but not perfect.
- The cable calibrations are not exact; they can be improved but will never be perfect.
- There is a large potential error from the human attempting to provide smooth motion as desired, but not succeeding perfectly. Cartesian orientations can be especially tricky to generate, but precise positions are challenging too.
- The experimental trajectory data of this section all assume that the ‘perfect’ simulation for comparison occurs with constant velocity. In the real world, the human naturally accelerates to constant velocity from rest and then decelerates to zero velocity (this can be seen in the α plot of Figure 9b, where the α slope starts and ends at zero). Of course, this can be modeled in simulation, but it is difficult to determine the level and time of acceleration and deceleration, which change with each new experiment.
- Cables 4 and 5 can easily jump off their pulleys, causing erroneous length readings. While this did not occur for the data presented (we repeated any cases when this did happen), this is a potential problem in practice.

Some of these error sources can be ameliorated by design improvements. In particular, the idea discussed at the end of Section 3.2, of placing a plate with a small hole for the cable near the nominal fixed cable points for each string pot, would help us to know the exact fixed cable points better and to avoid the cable/pulley errors, eliminating the need for iterative solutions altogether. A better design is required for moving cable connection points P_1 , P_2 , and P_3 to largely prevent their sliding relative to the tool. Clearly a precise calibration rig (a known cube for instance, placed precisely in the workspace) would help immensely in calibrating the cables, fixed cable connection points, and guiding the human in more precise motions; however, this is not realistic for sculpting or automated construction environments.

Despite these various error sources, we found reasonable results in the experiments. Section 4.2 presents the simulated Cartesian measurement resolution over various positions and orientations in the workspace. We found this measurement resolution to be grand overkill, generally down in the hundredths of mm ! This is simply based on how many digits we can reliably read from the string pot voltages. It is likely that a drifting voltage power supply to the

string pots and thermal expansion of the cables themselves may have more of an effect. For most, if not all, large-scale operations, the measurement resolution requirements will not be nearly so demanding as hundredths of *mm*.

Regarding absolute Cartesian accuracy, we initially observed errors of up to 50 *mm* or more for translations and up to 10° for rotations, comparing the experimental data with the off-line simulation, which was assumed to represent the real-world perfectly (which it cannot, of course). Upon improving our calibration procedures, we reduced this absolute Cartesian error *generally* to the 5-10 *mm* range for translations and less than 2° for rotations. We encountered absolute accuracies of 10-30 *mm* in the extreme (e.g. see Tables VII and VIII), but these relate to human error as much as systemic error. These numbers can apply to each Cartesian axis simultaneously, though we observed much better accuracies for many specific motions. Sculptor Helaman Ferguson believes that 10 *mm* accuracy is fine for large sculptures.

Regarding relative Cartesian accuracy (making Cartesian motions relative to defined reference poses on the material for sculpting), we expect lower errors than the absolute Cartesian accuracies since this mode removes the dependence on a well-known absolute world frame. Our lab experience indicates that the relative mode is preferable to absolute mode in our metrology system.

6. CONCLUSION

This article has presented a novel system for passive-cable-based Cartesian pose metrology. Six cables are connected to a moving body; six string pots (tensioning the cables via torsional springs) independently read the six cable lengths and analytical forward pose kinematics was presented to calculate the Cartesian pose in real time. Several important kinematics issues were also addressed related to cable-based metrology. The proposed system was introduced as a sculptor's aid, but there are many potential applications in manufacturing, rapid prototyping, robotics, and automated construction.

We presented experimental results, compared these with simulated motion results, and discussed the sources of error. Our experimental data and laboratory experience indicates that our system shows promise as a real-time, economical, accurate, safe, simple, and effective Cartesian pose metrology tool.

ACKNOWLEDGEMENTS

The first author gratefully acknowledges support for this work from the NIST Intelligent Systems Division, via Grant #70NANB2H0130.

REFERENCES

1. J.S. Albus, R. Bostelman, and N.G. Dagalakis, 1993, "*The NIST ROBOCRANE*", Journal of Robotic Systems, 10(5): 709-724.
2. P.D. Campbell, P.L. Swaim, and C.J. Thompson, 1995, "*Charlotte Robot Technology for Space and Terrestrial Applications*", 25th International Conference on Environmental Systems, San Diego, SAE Article 951520.
3. R.L. Williams II, P. Gallina, and J. Vadia, 2003, "*Planar Translational Cable-Direct-Driven Robots*", Journal of Robotic Systems, 20(3): 107-120.
4. Y.X. Su, B.Y. Duan, R.D. Nan, and B. Peng, 2001, "*Development of a Large Parallel-Cable Manipulator for the Feed-Supporting System of a Next-Generation Large Radio Telescope*", Journal of Robotic Systems, 18(11): 633-643.
5. R.G. Roberts, T. Graham, and T. Lippitt, 1998, "*On the Inverse Kinematics, Statics, and Fault Tolerance of Cable-Suspended Robots*", Journal of Robotic Systems, 15(10): 581-597.
6. R.V. Bostelman, 1990, "*Robot Calibrator*", Internal NIST Report.
7. M.R. Driels, W.E. Swayze, 1994, "*Automated Partial Pose Measurement System for Manipulator Calibration Experiments*", IEEE Transactions on Robotics and Automation, 10(4): 430-440.
8. J.W. Jeong, S.H. Kim, Y.K. Kwak, and C.C. Smith, 1998, "*Development of a Parallel Wire Mechanism for Measuring Position and Orientation of a Robot End-Effector*", Mechatronics, 8:845-861.
9. C. Ferguson, 1994, Helaman Ferguson: Mathematics in Stone and Bronze, Meridian Creative Group, Erie, PA.
10. R.V. Bostelman, 1993, "*String-Pot 2 (SP2) System*", Internal NIST Report.
11. H. Ferguson, 1998, "*Stone Sculpture from Equations*", IEEE International Symposium on Intelligent Control, Gaithersburg, MD, September 14-17: 765-770.
12. J.J. Craig, 1989, Introduction to Robotics: Mechanics and Control, Addison Wesley Publishing Co., Reading, MA.
13. R. Nair and J.H. Maddocks, 1994, "*On the Forward Kinematics of Parallel Manipulators*", International Journal of Robotics Research, 13(2): 171-188.
14. Z. Geng and L.S. Haynes, 1994, "*A 3-2-1- Kinematic Configuration of a Stewart Platform and its Application to Six Degree of Freedom Pose Measurements*", Robotics & Computer-Integrated Manufacturing, 11(1): 23-34.
15. P. Zsombor-Murray, 2000, "*Forward Kinematics of the 6-3 (3-2-1) Platform with a Succession of Three Tetrahedral Constructions using Three Sphere Intersections Reduced to Line \cap Sphere*", course notes.
16. R.L. Williams II, 2002, "*Six-Cable Hand-Directed Sculpting Metrology Tool: Modeling and Implementation*", Internal NIST Report.